

A Transmit Lens Array With High-Gain and Beam-Steering Capabilities at Submillimeter Wavelengths

Alonso-Delpino, Maria; Bosma, Sjoerd; Jung-Kubiak, Cecile; Bueno, Juan; Chattopadhyay, Goutam; Llombart, Nuria

DOI

[10.1109/TTHZ.2023.3321253](https://doi.org/10.1109/TTHZ.2023.3321253)

Publication date

2024

Document Version

Final published version

Published in

IEEE Transactions on Terahertz Science and Technology

Citation (APA)

Alonso-Delpino, M., Bosma, S., Jung-Kubiak, C., Bueno, J., Chattopadhyay, G., & Llombart, N. (2024). A Transmit Lens Array With High-Gain and Beam-Steering Capabilities at Submillimeter Wavelengths. *IEEE Transactions on Terahertz Science and Technology*, 14(1), 64-75.
<https://doi.org/10.1109/TTHZ.2023.3321253>

Important note

To cite this publication, please use the final published version (if applicable).
Please check the document version above.

Copyright

Other than for strictly personal use, it is not permitted to download, forward or distribute the text or part of it, without the consent of the author(s) and/or copyright holder(s), unless the work is under an open content license such as Creative Commons.

Takedown policy

Please contact us and provide details if you believe this document breaches copyrights.
We will remove access to the work immediately and investigate your claim.

Green Open Access added to TU Delft Institutional Repository

'You share, we take care!' - Taverne project

<https://www.openaccess.nl/en/you-share-we-take-care>

Otherwise as indicated in the copyright section: the publisher is the copyright holder of this work and the author uses the Dutch legislation to make this work public.

A Transmit Lens Array With High-Gain and Beam-Steering Capabilities at Submillimeter Wavelengths

Maria Alonso-delPino , Senior Member, IEEE, Sjoerd Bosma , Member, IEEE, Cecile Jung-Kubiak , Senior Member, IEEE, Juan Bueno , Goutam Chattopadhyay , Fellow, IEEE, and Nuria Llombart , Fellow, IEEE

Abstract—This article introduces a novel transmit lens array with beam-steering capabilities for submillimeter-wave space instruments. The transmit array consists of two sparse silicon lens antenna arrays connected by a waveguide array, in which active components can potentially be integrated, arranged in a hexagonal grid. The upper lens array is mechanically actuated to achieve dynamic beam-steering. The bottom lens array is fed coherently by a quasi-optical (QO) power distribution lens antenna. This antenna is capable of distributing power to a multipixel lens array in a hexagonal configuration with a power coupling efficiency of approximately 60%. The transmit lens array and QO power distribution lens antennas are based on a recently developed multimode leaky-wave feed, which results in lens antenna aperture efficiencies of nearly 80%. A model based on high-frequency techniques has been implemented to design and optimize the complete architecture, allowing to evaluate its directivity and gain. We have fabricated and measured a prototype based on seven-lens elements with excellent agreement to the performances estimated by the model. This article demonstrates for the first time an array architecture that reaches 36 dBi directivity, 32 dBi gain, and $\pm 25^\circ$ scanning with 3 dB scan loss over a 450–650 GHz band.

Index Terms—Leaky-wave antenna, quasi-optical (QO) power distribution, scanning lens phased array, submillimeter-wave antennas, THz arrays, transmit lens array.

I. INTRODUCTION

SUBMILLIMETER-WAVE heterodyne instruments primarily rely on the mechanical actuation of a large telescope system with bulky and power-hungry motors to realize beam-steering [1], [2], [3], [4]. To enable future space missions with

severe mass and power constraints, dynamic beam-steering capabilities of high-gain beams are required in a more compact form factor [5]. Phased arrays, extensively used in the microwave regime, would be an ideal candidate for these missions due to their compact, low-profile architecture. Now that integrated silicon technology is reaching ft/fmax in the terahertz regime, one can envision its use at such high frequencies [6], [7], [8], [9]. However, high-gain, fully sampled arrays suffer both from physical constraints with packaging and high losses in the power distribution network [6], [7], [8], [9], [10], [11].

We recently proposed a sparse lens phased array [12] capable of wide-angle beam-steering ($\pm 25^\circ$) of a very high-gain beam (>35 dBi) using an electro-mechanical phase shifting network. The sparse array factor (AF) can be steered electronically using IQ-mixers as demonstrated in [13] or via microelectromechanical systems (MEMS) phase shifters [14], both integrated in waveguides. To control the grating lobe level, the element pattern is steered dynamically by a small (in the order of a few millimeters) translation of the lens array from their feeds. The sparsity of this lens array architecture greatly reduces the integration complexity with respect to a fully sampled array [6], [7], [8], [9] since it reduces the number of active elements by $\sim (2D_e/\lambda_0)^2$, being D_e the diameter of the element aperture and λ_0 the wavelength in free-space. Compared to a conventional QO system of the same diameter and f -number, the lens phased array has a lower profile, improves the beam-steering performance while requiring a significantly smaller mechanical displacement [12]. This has been realized using an integrated piezo-motor as proposed in [12], [13], [14], and [15]. As demonstrated, this technology can translate this lens array with accuracies in the nanometer scale and exhibit minimal power consumption and heat generation.

There are not many broadband and efficient solutions to distribute power over large arrays at submillimeter-wave frequencies. Waveguide splitters can be efficient for a limited number of elements that are closely spaced [16], [17]. However, at these frequencies, losses increase rapidly with the number of elements and the spacing of the array [16], [17], [18], [19]. In the example in [19], the total loss for a 2×2 power distribution at 1.37 THz was 13–20 dB. Another option is to use phase-gratings, currently used for local oscillator power distribution to hot electron

Manuscript received 29 June 2023; revised 1 September 2023; accepted 18 September 2023. Date of publication 13 October 2023; date of current version 5 January 2024. (Corresponding author: Maria Alonso-delPino.)

Maria Alonso-delPino, Sjoerd Bosma, Juan Bueno, and Nuria Llombart are with the Terahertz Sensing Group, Technical University of Delft, 2628 CD Delft, The Netherlands (e-mail: m.alonsodelpino@tudelft.nl; s.bosma@tudelft.nl; j.buenolopez@tudelft.nl; n.llombartjuan@tudelft.nl).

Cecile Jung-Kubiak is with the Advanced Optical and Electromechanical Microsystem Group, Jet Propulsion Laboratory, California Institute of Technology, Pasadena, CA 91109 USA (e-mail: cecile.d.jung@jpl.nasa.gov).

Goutam Chattopadhyay is with the Submillimeter-Wave Advanced Technology Group, Jet Propulsion Laboratory, California Institute of Technology, Pasadena, CA 91109 USA (e-mail: goutam.chattopadhyay@jpl.nasa.gov).

Color versions of one or more figures in this article are available at <https://doi.org/10.1109/TTHZ.2023.3321253>.

Digital Object Identifier 10.1109/TTHZ.2023.3321253

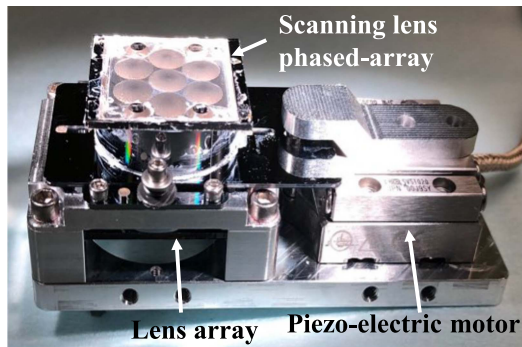


Fig. 1. Photograph final transmit lens array fixture showing the top scanning lens phased array and bottom lens array with the piezo-motor.

bolometer (HEB) and superconductor-insulator-superconductor (SIS) detector technology [20], [21], [22]. These gratings are only feasible over a narrow-band and are not scalable to large arrays [22]. To overcome these limitations, we propose a novel quasi-optical (QO) power distribution architecture [23], [24], [25] that provides efficient and broadband power distribution and yet scalable with the number of elements and large apertures. Moreover, this architecture provides amplitude and phase coherency among the elements. This QO architecture is based on a near-field coupling between the collimated beam generated by a QO antenna and the collimated beams of a sparse lens array.

In this article, we develop a lens phased array that is coherently fed using a QO power distribution architecture. This results in a transmit lens array architecture in which the bottom lens array handles the power distribution while the top lens array radiates a high-gain beam with scanning capabilities. Overall, the proposed architecture results in a high-gain steerable beam over 450–650 GHz band. In [15], we presented for the first time a single silicon lens antenna integrated with a piezo-electric motor. In [12], we presented the lens-phased array concept with a prototype of a single antenna array embedded element and its scanning capabilities with the piezo-electric motor. In [13], we presented a 4×1 lens phased array at 100 GHz using plastic lenses with dynamic beam-steering. Some preliminary analysis and prototypes can be found in conference papers in [23], [24], and [25]. However, this article entails the detailed model, design, fabrication, assembly, and characterization of a seven-element transmit lens array prototype using silicon micromachining techniques at 500 GHz for the first time, as shown in Fig. 1.

The rest of this article is organized as follows. First, we explain the proposed geometry and dimensions in Section II. Section III presents the semianalytical model to design and optimize the transmit lens array and its performance. The fabrication and assembly of a 450–650 GHz of a seven-element transmit lens array is shown in Section IV. Its characterization is presented in Section V. Finally, Section VI concludes this article.

II. TRANSMIT LENS ARRAY ARCHITECTURE

The proposed transmit lens array architecture is shown in Fig. 2. The transmit lens array is composed of two sparse lens

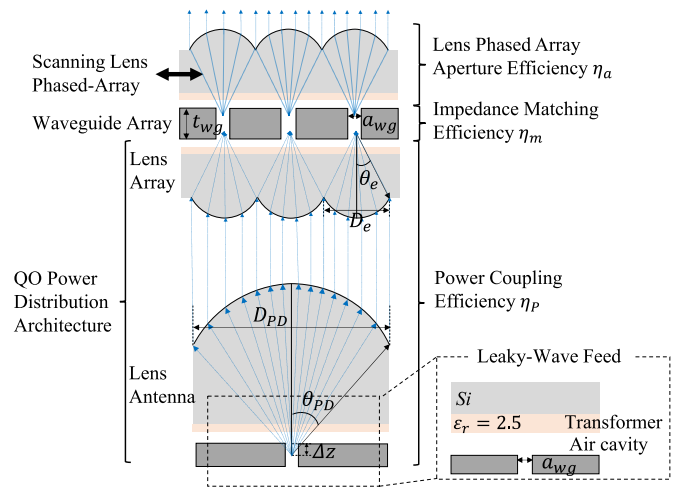


Fig. 2. Proposed transmit lens array and QO power distribution architecture. The main geometrical parameters are provided together with the different efficiency terms.

arrays. The bottom lens array coherently couples the radiation from a QO power distribution antenna to an array of waveguides, where active components can potentially be integrated. The top lens array combines coherently all the received power from the waveguide array into a narrow beam that can be scanned over a certain field of view [12]. In the following sections, a detailed description of these two main parts is provided.

A. QO Power Distribution Architecture

The QO power distribution is constituted by a large silicon lens antenna that radiates a collimated, nearly uniform beam at its circular aperture, with diameter D_{PD} . This aperture has the same size as bottom N -element lens array each with a circular aperture of diameter D_e . The lens antennas constituting this array are also designed to form a collimated uniform beam to maximize the power coupling between both geometries, see Fig. 2. If all the lens antennas had an ideal 100% aperture efficiency, the only loss in this architecture would be related to how well the circular aperture of the large lens is sampled by smaller circular apertures of the lens array $\eta_{\text{fill factor}} = N \left(\frac{D_e}{D_{PD}} \right)^2$. When lenses of equal diameter are considered, a lens array with a hexagonal lattice is the one that provides the higher coverage of a circular area compared to a rectangular lattice. For instance, the fill factor efficiency for a seven-element hexagonal array is $\eta_{\text{fill factor}} \approx 78\%$ and reaches up to 90.7% as the number of elements increase.

This architecture is not just a scalable power distribution solution for arrays with a high number of elements, but also for arrays with large apertures. To maintain a low-profile, the architecture can be scaled up by tiling subarrays, as shown in Fig. 3. Instead of illuminating the entire aperture of the transmit-array D_a , D_{PD} only illuminates a subarray composed of D_e apertures. This reduces its profile by D_a/D_{PD} compared to a standard QO-system of the same f -number.

The initial demonstration of the lens antenna of the QO power distribution architecture operating at 450–650 GHz was shown

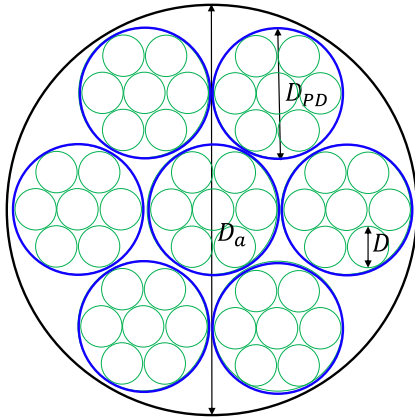


Fig. 3. Example of subarray tiling of the QO lens antenna aperture D_{PD} to synthesize the aperture of the transmit array D_a .

TABLE I
OPTIMIZED TRANSMIT LENS ARRAY AND QO POWER DISTRIBUTION
ANTENNA DIMENSIONS

Parameter	Value
D_{PD}	15.4 mm
θ_{PD}	18.5°
Δz	-1.2 mm
D_e	5.14 mm
θ_e	17.25°
a_{wg}	362 μm
t_{wg}	300 μm

in [25], with the focus on maximizing its aperture efficiency. This antenna was realized using a silicon lens truncated to θ_{PD} fed by a multimode leaky-wave waveguide feed [12]. The feed was composed of a grounded open square waveguide of dimensions a_{wg} , an air cavity of $\lambda_0/2$, and a dielectric transformer slab of thickness $\lambda_0/4\sqrt{\epsilon_m}$, where $\epsilon_r = 2.5$. Its geometrical parameters are indicated in Fig. 2 and Table I. It was demonstrated in [25] that the aperture efficiency of this lens antenna is above 80% across the 450–650 GHz. The radiation pattern inside the silicon lens resembles a top-hat pattern: nearly uniform until $\theta < 18^\circ$. The same lens antenna is used in this work to illuminate coherently a seven-element hexagonally arranged lens array. This is the bottom lens array in Fig. 2, which in this demonstration has the same equivalent diameter D_{PD} as lens antenna. Despite the equal diameter of the lens antenna and bottom array, most of the power is coupled from the lens antenna to the array. This is due to their close proximity, in the near-field region, where there is negligible field spreading. The same leaky wave feed is used in the lens array to ensure a high coupling coefficient between both antennas via uniform collimated beams. In the following section, we present a detailed analysis of the power coupling efficiency from the lens antenna to the bottom lens array.

B. Lens-Phased Array Architecture

The second part of the proposed transmit lens array (see top array in Fig. 2) consists of a mechanically actuated lens

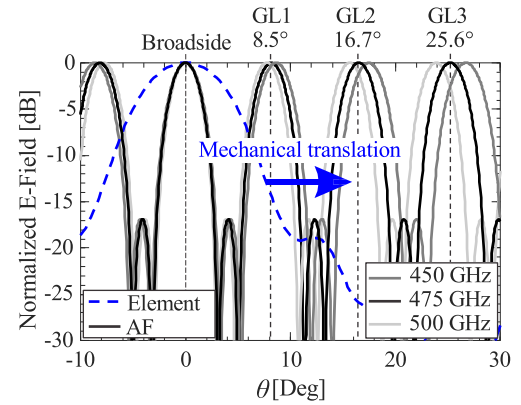


Fig. 4. Radiation pattern of the lens-transmit array showing the translation of the element pattern towards a grating lobe of the AF at 475 GHz in the H Plane. The AF at 450 GHz and 500 GHz is displayed in grey to exhibit its frequency dispersion.

phased-array, which enables dynamic beam-steering of a high-gain beam. The lens phased array has the same geometry as described in [12] and it is symmetrical w.r.t the bottom one described previously. Both lens arrays are connected through an array of square waveguides of length t_{wg} , as shown in Fig. 2.

In order to achieve continuous angular beam-steering, the combination of an electronic phase shifting network (scanning of the array factor) and a mechanical translation of the lens array (scanning of the element pattern) is required [12], [13]. In this work, the electronic phase shifting network has not been included in the prototype, in order to first assess the raw performance and coherency of the overall transmit lens array. Therefore, it is not possible to steer the array factor using our prototype. We can partially demonstrate the steering capabilities by using only the mechanical steering of the element factor to a certain number of discrete angles.

The mechanical steering is achieved via the translation of the lens array using the piezo-electric motor from [12], [13], [15]. The discrete angles that this configuration can be steered to are those where the element pattern maximum coincides with one of the array factor's grating lobes. This is visualized in Fig. 4. For the proposed case with a seven-elements hexagonal grid and a periodicity of $10\lambda_0$, the number of discrete scanning angles in the H plane for 30° scanning (up to 3 dB scan loss) are three, as indicated in the same figure. The location of these grating lobes changes with frequency.

Nonetheless, a feasible strategy to implement the electronic beam-forming network in the waveguide array is the integration of phase shifters in the 450–650 GHz band, as the ones in [14] based on MEMS technology. Another possibility is to realize QO power distribution and the phase shifting network at a lower frequency where more phase-shifting devices and RF power are available. For example, at H-band, the proposed QO power distribution could couple to an array of vector network modulators based on I/Q-mixers as in [12] or attenuator-based modulators [26]. After that, each element would be coupled to a power amplifier and a doubler to reach the 450–650 GHz. Thanks to the sparsity of the proposed array, i.e., interelement

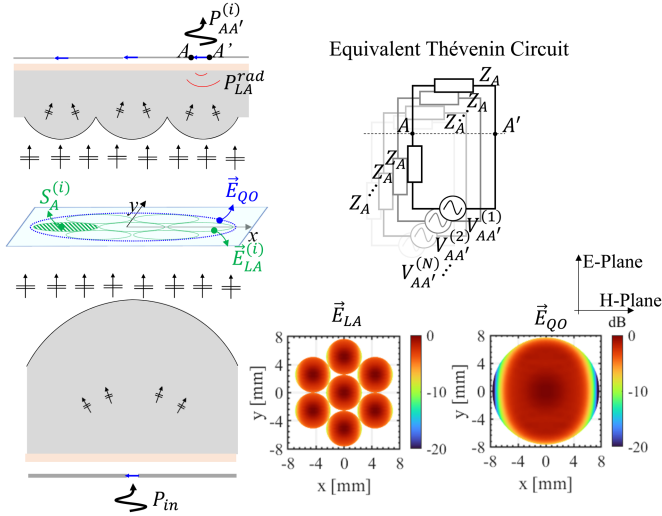


Fig. 5. (Left) Schematic of the QO power distribution architecture. (Top right) Equivalent Thévenin circuit for the lens array evaluated in reception. (Bottom right) Electric field of the lens array and quasi-optical power distribution lens antenna on the aperture plane at 550 GHz.

spacing of 5.14 mm, and the vertical integration capabilities of the silicon micromachined stack of wafers, the different MMIC could be integrated in-between the two lens antenna arrays. This approach is similar to the methodology applied in [27], where a lens antenna was integrated with a 1.9 THz tripler in a silicon micromachined package. Vertical-to-horizontal waveguide transitions could be employed to interconnect the antennas with each phase-shifter, while lateral interconnections are envisioned for the routing of the dc bias and IF lines.

III. DESIGN AND PERFORMANCE OF A SEVEN-ELEMENT TRANSMIT LENS ARRAY

The elements of the proposed transmit lens arrays are large in terms of the wavelength, which results in unviable full-wave simulations. To tackle this limitation, we developed a quasi-optical model to assess its performance (efficiency and radiation patterns) and optimize this architecture. We model the efficiency of the overall transmit lens array as the product of three main contributions, as highlighted in Fig. 2: the power coupling efficiency to the array of waveguides η_c , the impedance matching efficiency between the two lens arrays η_m , and the aperture efficiency of the lens phased array η_{ap} . The overall efficiency encompasses the aforementioned terms, and it is referred to as the transmit lens array efficiency η_{TA} . Next, these efficiency terms are detailed individually.

A. Power Coupling Efficiency Analysis

The first step is to calculate how much power is received at the input of the waveguide array, which is at the antenna terminals AA' indicated in Fig. 5. This power is referred as $P_{AA'}^{(i)}$ where $i = 1 \dots N$ indicates the corresponding waveguide terminal and N is the number of elements of the array (in this demonstration $N = 7$). Then, the power coupling efficiency, η_p is defined as the summation these received powers, normalized to the input

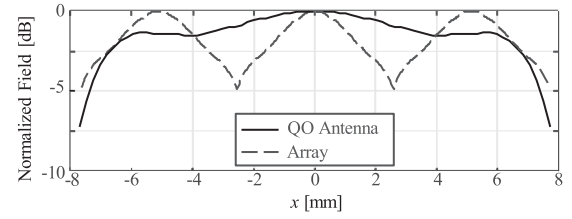


Fig. 6. Electric-field distribution at the aperture of the QO power distribution lens antenna \vec{E}_{QO} and the lens array \vec{E}_{LA} at 550 GHz in the E plane at 550 GHz.

power P_{in} , (see Fig. 5) of the QO power distribution lens antenna

$$\eta_p = \frac{1}{P_{in}} \sum_{i=1}^N P_{AA'}^{(i)} \quad (1)$$

To evaluate the power received in each waveguide, we apply an analysis of the antennas in reception, analogous to [25]. This approach allow us to evaluate the coupling efficiency without the need for more time-consuming physical optics simulations as in [26]. The problem is analyzed in reception by using the equivalent Thévenin circuits of Fig. 5, one per waveguide, and assuming a matched load (the mismatch is considered in the following section). The antenna impedance of all the elements is identical and indicated as Z_A . Then, the received power at each lens terminal is defined as

$$P_{AA'}^{(i)} = \frac{|(V_{AA'} I)^{(i)}|^2}{16 P_{LA}^{rad}} \quad (2)$$

where P_{LA}^{rad} is the power radiated by the leaky-wave feed of the antenna element of the array in the infinite dielectric silicon medium, and it is proportional to I^2 . $V_{AA'}$ is the open circuit voltage used in the Thévenin circuits of Fig. 5.

The open circuit voltage can be calculated as the reaction integral between the incident electric field \vec{E}_{QO} associated to the QO power distribution lens and the field radiated by the lens antenna array element in transmission $\vec{E}_{LA}^{(i)}$ over a closed surface surrounding the antenna

$$(V_{AA'} I)^{(i)} = \frac{2}{\zeta_0} \iint_{S_A^{(i)}} \vec{E}_{LA}^{(i)} \cdot \vec{E}_{QO} dA \quad (3)$$

where ζ_0 is the intrinsic impedance of the air medium. For the specific case of the elliptical lens antenna and choosing the surface plane on the top of the lens antenna aperture $S_A^{(i)}$. The fields radiated by the lens array $\vec{E}_{LA}^{(i)}$ and quasi-optical power distribution lens antenna \vec{E}_{QO} on the aperture plane $S_A^{(i)}$ (indicated in Fig. 6) are calculated using geometrical optics technique as in [28]. The lens of the QO power distribution lens antenna is large in terms of the wavelength and consequently, it resides in the far-field of the leaky-wave feed. The lenses of the array are in the order of a few wavelengths; hence, for those, the near-field effects have been considered, as in [12].

This model has been used to optimize the power received by the transmit array as a function of the truncation angle θ_{PD}

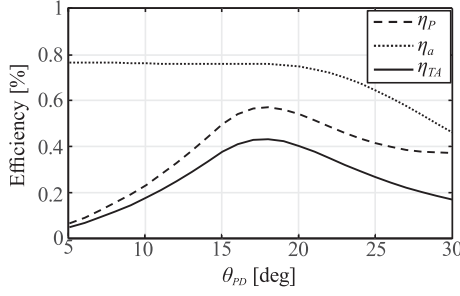


Fig. 7. Power coupling efficiency, aperture efficiency, and transmit lens array efficiency as a function of the lens antenna truncation angle at 550 GHz

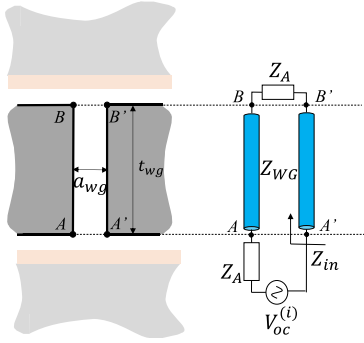


Fig. 8. Schematic of a single element impedance matching efficiency equivalent model and circuit.

of the QO power distribution lens antenna at 550 GHz. The power coupling efficiency as a function of the truncation angle is shown in Fig. 7. It is maximum for a truncation angle of 17.5° reaching almost 60%. Note that a quarter-wavelength parylene-C ($\epsilon_r \approx 2.62$) has been assumed for the calculations. For small truncation angles, most power will be lost due to spill-over, while for larger truncation angles, the uniformity of the aperture field is too low to provide good coupling to all lenses.

B. Impedance Matching Efficiency

The impedance matching efficiency quantifies a potential loss of power associated to an impedance mismatch between the top and bottom lens arrays. Since the mutual coupling between the array elements is negligible, this efficiency can be simplified to the evaluation of one end-end waveguide transition shown in Fig. 8. This transition includes the bottom and top leaky-wave stratifications radiating into an infinite silicon medium, the waveguide square apertures and a straight waveguide piece. This structure is represented using the equivalent circuit shown in Fig. 8 (Right). It is composed by the same $V_{AA'}^{(i)}$ voltage source described in (4), the leaky wave antenna's input impedance Z_A , and a transmission line of length t_{wg} with a characteristic impedance of the TE_{10} mode $Z_{WG} = k\zeta_0/\beta$, where β is the propagation constant in the waveguide. Thus, the impedance matching efficiency is defined as

$$\eta_m = 1 - \left| \frac{Z_{in} - Z_A^*}{Z_{in} + Z_A} \right|^2 \quad (4)$$

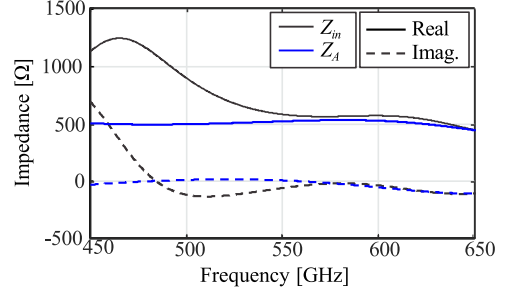


Fig. 9. Real and imaginary part of the input impedance seen from AA' plane and the antenna impedance as a function of the frequency.

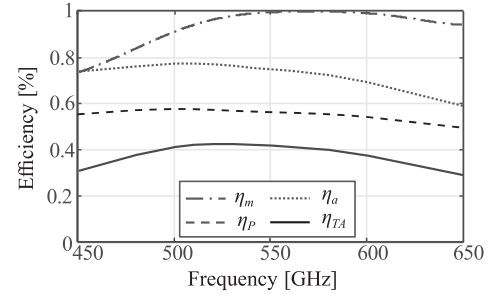


Fig. 10. Power coupling efficiency, aperture efficiency, impedance matching efficiency, and transmit lens array efficiency as a function of the frequency.

where $Z_{in} = Z_{WG} \frac{Z_A + jZ_{WG} \tan(\beta t_{wg})}{Z_{WG} + jZ_A \tan(\beta t_{wg})}$. The simulated antenna impedance and the calculated input impedance as a function of the frequency are shown in Fig. 9. The input impedance resembles the impedance of the antenna, exhibiting a constant real value of approximately 500Ω and an imaginary part also close to 0Ω over the high frequency band. In this part of the spectrum, the impedance match efficiency is above 95%, as shown in Fig. 10. However, the lower part of the frequency spectrum is affected by the proximity of the frequency cut-off of the square waveguide (413 GHz). In this region, the matching efficiency drops considerably down to 78% at 450 GHz, as shown in Fig. 10.

C. Lens Phased Array Aperture Efficiency

The aperture efficiency of the lens phased array—the top part in Fig. 2—is defined as the ratio of power received at the antenna terminals BB' from a plane wave incident on the lens to the power in the plane wave (limited to the lens' area), as illustrated in Fig. 11

$$\eta_a = \frac{P_{BB'}}{P_{pw}} \quad (5)$$

The plane-wave power in the area $A_{TA} = \pi(\frac{D_{PD}}{2})^2$ is $P_{pw} = A_{TA}|E_{pw}|^2/(2\zeta_0)$. $P_{BB'}$ is the power received by the transmit array on the terminals BB' induced by a plane-wave excitation is calculated as

$$P_{BB'} = \frac{|V_{BB'} I|^2}{16P_{TA}^{rad}} \quad (6)$$

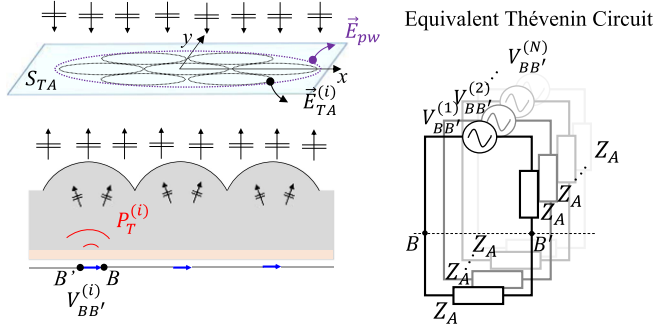


Fig. 11. Schematic of the top lens antenna array coupling to a plane wave and its Thévenin circuit.

and in this case

$$V_{BB'} I = \frac{2}{\xi_0} \iint_{S_{TA}} \vec{E}_{TA} \cdot \vec{E}_{pw} dS \quad (7)$$

where \vec{E}_{TA} is the aperture field of the lens transmit array $\vec{E}_{TA} = \sum_{i=1}^N \vec{E}_{TA}^{(i)}$, and $\vec{E}_{TA}^{(i)}$ is the aperture field of the array element. In this case, where top and bottom array are connected through a square waveguide, we can add the weights calculated from the $V_{AA'}^{(i)}$ from (3) $\vec{E}_{TA}^{(i)} = \vec{E}_{LA}^{(i)} V_{AA'}^{(i)}$. Last, P_{TA}^{rad} is the total power radiated by the leaky-wave feed of the lens array in the semi-infinite silicon medium $P_{TA}^{rad} = P_{LA}^{rad} \sum_{i=1}^N |V_{AA'}^{(i)}|^2$.

The top lens phased array efficiency as a function of the truncation angle is shown in Fig. 7. The aperture efficiency remains constant for small truncation angles due to the uniformity of the power distribution, which is almost 80% until almost 20°. For larger truncation angles, it rapidly decreases because only the central array element is efficiently illuminated by the large lens.

D. Transmit Lens Array Performance

Finally, the total transmit lens array efficiency is defined as the product of the three previously analyzed efficiency terms

$$\eta_{TA} = \eta_c \eta_m \eta_a. \quad (8)$$

This efficiency takes into account the entire transmit lens array architecture: from the power distribution lens to the bottom array, through the waveguide and radiated into free space by the top array, including the losses due to spill-over and reflections at the various lens-air and air-lens interfaces. As shown in Fig. 7, the maximum is around 43% achieved for $\theta_B = 18.5^\circ$ and the maximum coincides with the maximum of η_c .

At the optimized truncation angle, one can check the amplitude and phase of the $V_{AA'}^{(i)}$ obtained in interface AA'. Note that due to the symmetry of the array, only three unique induced voltages are shown (the numbering of the elements is shown in the inset Fig. 12). A maximum power difference of 2.6 dB is achieved across the array and the maximum phase is 6°, as shown in Fig. 12(a). The resulting radiation pattern based on this weight distribution is shown in Fig. 12(b) and is compared to

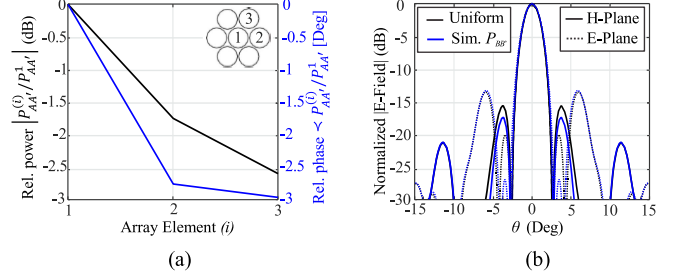


Fig. 12. (a) Power-coupling to each waveguide element relative to the central element. (b) Resulting array pattern based on the weight distribution computed from the \vec{E}_{TA} compared with the ideal uniform case at 550 GHz.

the uniform case. The effect of these variations in the resulting radiation pattern is very small. These simulated patterns were obtained by multiplying the simulated element pattern by the array factor, including the appropriate weight $V_{AA'}$.

Since the result of this nonuniform illumination between the elements results on a coherent array illumination with negligible tapering, the proposed configuration can be used to enable dynamic beam-steering using the scanning lens phased array concept [12]. Instead, if the array was to be used as a focal plane array, the obtained power difference will need to be considered when using this architecture to drive mixers or multipliers and a different optimization goal might be needed to equalize the power level among the elements.

After fixing the truncation angle at the optimum, the transmit array efficiency and its compounding factors are plotted as a function of frequency from 450–650 GHz. The results in Fig. 10 show an efficiency above 30% in the entire band and above 40% between 500–575 GHz.

The optimized geometrical parameters of the lens transmit array and quasi-optical power distribution lens antenna are shown in Table I. These are the parameters that have been used to develop the prototype that is detailed in the following section.

IV. PROTOTYPE FABRICATION AND ASSEMBLY AT 450–650 GHz

We have developed a 450–650 GHz seven-element transmit lens array prototype and the QO power distribution lens antenna. The photographs of the prototypes are shown in Figs. 1, 13, and 14. The transmit array is entirely synthesized in micromachined silicon, combining deep reactive ion etching (DRIE), diamond turning, and laser-machining techniques. A sketch of the silicon assembly and some photographs of it are shown in Fig. 13. The bottom lens array of the assembly is used to couple the radiation from the QO power distribution lens antenna to an array of waveguides. The top lens array assembly is used to realize the lens phased array. For the beam-steering, the top lens array is connected to a piezo-electric motor through a small metal fixture as in [12] (see Fig. 1). The piezo-electric motor translates the top lens array with respect to the waveguide array in the H plane, achieving a translation range of ± 1.25 mm, and thus, a beam-steering of around $\pm 25^\circ$.

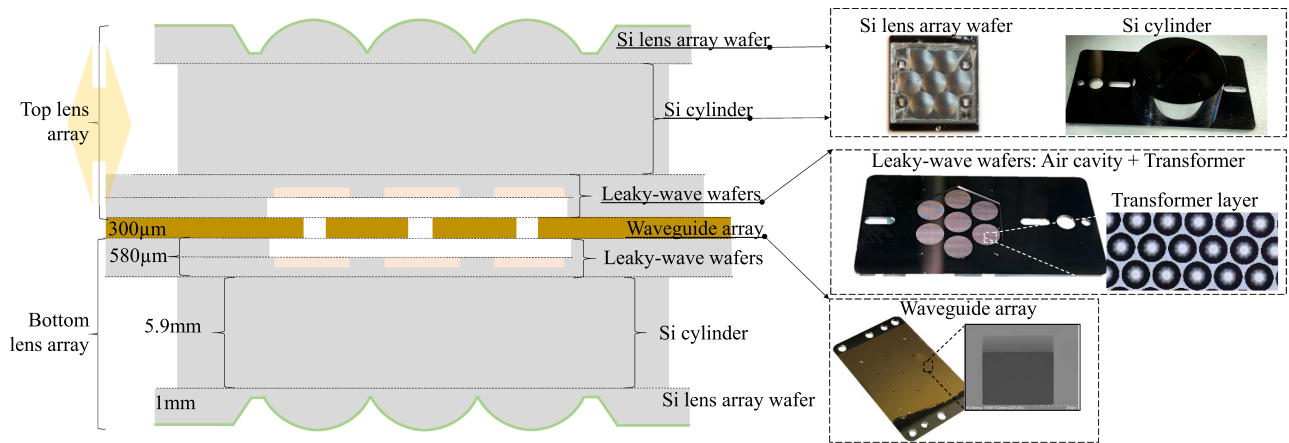


Fig. 13. (Left) Schematics of the silicon assembly of the transmit lens array. (Top-right) Photographs of the top and bottom view of a lens Si lens array wafer and Si cylinder assembled on the leaky wave wafers. (Middle-right) Photograph from the leaky wave wafers assembled showing the air cavity and transformer layer. The inset is a photograph taken by the microscope of the artificial dielectric transformer layers synthesized with $73 \mu\text{m}$ diameter holes over a $79 \mu\text{m}$ lattice. (Bottom-right) Photograph of the waveguide array wafer, the inset shows an SEM photograph of one of the square waveguides of $362 \mu\text{m}$ side.

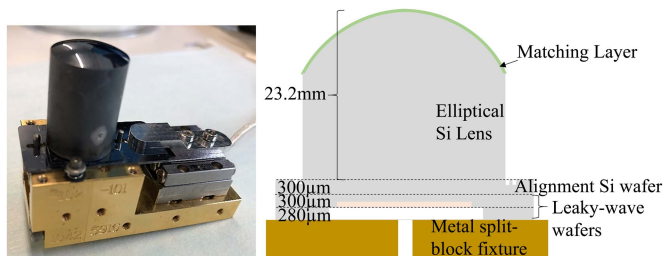


Fig. 14. (Left) Photograph of the QO power distribution lens antenna. (Right) Schematics of the silicon microfabricated wafers and lens assembly.

The bottom lens array distributes the power into seven microfabricated square waveguides, and consists of a Si lens array wafer, a Si cylinder, two leaky wave feed wafers and a waveguide array wafer. The lens array is fabricated in high resistivity ($> 10 \text{ k}\Omega \cdot \text{cm}$) silicon using laser ablation.¹ A parylene-C ($\epsilon_r \approx 2.62$) quarter-wavelength matching layer at the frequency of 550 GHz is deposited on the top of the lens array [12]. The lens array has four alignment holes that are used to align the array to rest of the bottom lens array silicon stack. The lens array is glued to a high resistivity, 5.9 mm thick silicon cylinder of 19.2 mm diameter, which is used as a spacer to place the antenna feed array at the focus of the lens array. The cylinder is machined by diamond turning² and contains an engraved circular mark of $70 \mu\text{m}$ diameter and $6 \mu\text{m}$ depth on the center of both sides of the cylinder. These circular marks are then used to align the cylinder with the laser in order to ablate pin pockets on one side of the cylinder and alignment markers on the other side. The silicon pin pockets are used with the silicon pensile pins [12] to align the cylinder to two leaky-wave silicon wafers (within $10 \mu\text{m}$) whereas the alignment markers are used to position the lens array accurately (within $15 \mu\text{m}$) and glue it onto the cylinder (as shown in Fig. 13). Although we used a stack of Si wafers in the past [12] to make the lens array extension, in this assembly,

¹[Online]. Available: <https://www.veldlaser.nl/en/>

²[Online]. Available: <https://www.sumipro.nl/>

we replaced them with a single cylinder of 5.9 mm thickness. We noticed that such a stack of wafers lead to unwanted reflections among the large number of interfaces present in the assembly. Further details are given in the Appendix.

The waveguides and the leaky wave feed are fabricated using the same DRIE process described in [30]. The leaky wave feed is composed of an air cavity of thickness $280 \mu\text{m}$ and a transformer layer of permittivity 2.5 and thickness of $88 \mu\text{m}$ as in [12]. The air-cavity is synthesized on a $300 \mu\text{m}$ silicon wafer that is etch down to a thickness of $280 \mu\text{m}$. The transformer layer is synthesized on a $300 \mu\text{m}$ high resistivity silicon wafer by etching holes of $73 \mu\text{m}$ in diameter and $88 \mu\text{m}$ depth over a triangular lattice of $79 \mu\text{m}$ as in [12], see inset in Fig. 13. The waveguide array is fabricated on a $300 \mu\text{m}$ silicon wafer that is gold-plated. The inner walls of the waveguides are very smooth, as can be seen in the scanning electron microscope (SEM) image (see inset Fig. 13). The waveguides and cavity are aligned and glued together using silicon pensile pins as in [12]. The assembled bottom array is aligned to the metal fixture using 1.5 mm dowel pins to assure a reliable alignment within $25 \mu\text{m}$ accuracy between the bottom and top lens arrays.

The top lens array consists of two leaky-wave feed wafers, a Si cylinder and a lens array wafer, all synthesized and assembled in the same manner as the bottom lens array. The leaky-wave feed wafers are connected to the metal fixture that translates the overall top lens array via the piezo-electric motor. The top array is aligned to the metal fixture using 1.5 mm dowel pins in the E plane whereas we use the piezo-electric motor in the H plane to steer the radiation beams. To maintain alignment while the piezo-electric motor moves, these pins are used as rails where the piezo-electric motor performs the push/pull of the lens array across the axis of movement. The top array is fixed to the metal fixture using spring loaded screws that ensure good contact between the bottom and top arrays during the piezo-electric motor movement.

The QO power distribution lens antenna consists of a single elliptical lens of diameter 15.4 mm, an alignment Si wafer, the two leaky-wave feed wafers, and a metal split-block fixture to

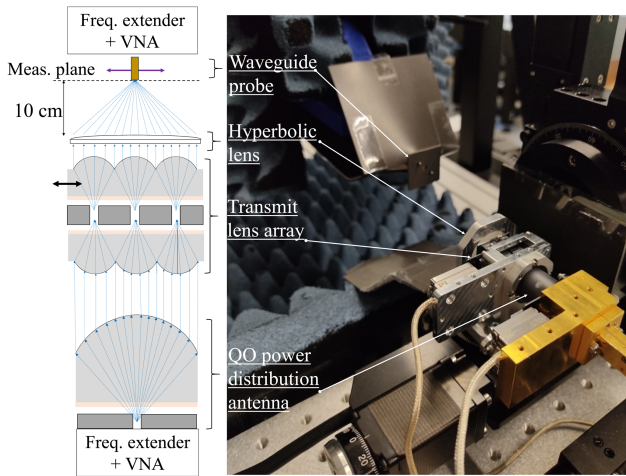


Fig. 15. Schematics and photograph of the transmit lens array measurement setup.

which all components are assembled. The fabricated prototype is shown in Fig. 14. The silicon lens, coated with an antireflective coating is optically aligned and glued to an alignment Si layer. This layer is synthesized on a high resistivity $300\ \mu\text{m}$ thick silicon wafer that has engraved a series of square patterns to enable the optical alignment of the lens. The leaky wave feed is identical to the one used in [12]. The alignment Si layer is aligned to the leaky wave feed using the aforementioned silicon pensile pins and glued. The fabrication, assembly, and characterization of the stand-alone QO power distribution lens was explained in [25], showing a very good agreement with simulations.

V. MEASUREMENT RESULTS

The fabricated prototype has been characterized using an ad-hoc measurement antenna setup, which consists of a planar computer numerical control (CNC) scanner and a performance network analyzer (PNA) in combination with a pair of frequency extenders in the WR2.2 band. Unfortunately, due to unavailability of WR 1.5 frequency extenders at the Technical University of Delft Laboratory, the transmit lens array prototype could not be measured at the highest frequency band (above 500 GHz). The measurement setup photograph is shown in Fig. 15.

To facilitate the antenna characterization of a high-gain antenna in a planar setup, a hyperbolic lens is used in front of the transmit lens array to focus the beam on a spot at 10 cm distance [13], [25]. This solution provides a smaller scanning area to reduce the scanning time, thus, facilitates a dynamic alignment of the different components, similar to what was done in [13] and [25]. Moreover, we can utilize a far-field evaluation to characterize the setup losses and increase the dynamic range of the overall measurement setup with respect to near-field planar scanning.

The waveguide flange of the frequency extender is placed at the focus of the hyperbolic lens (at 10 cm), and it is used to measure the radiation patterns in that spot. A thin sheet of Eccosorb absorber is placed the surrounding the waveguide flange aperture to mitigate the multiple scattering and reflections propagating

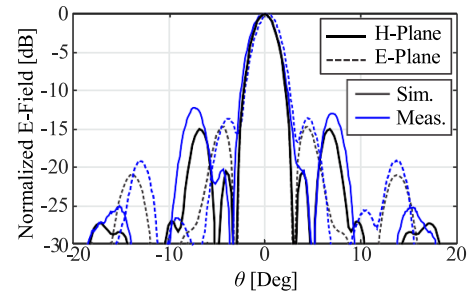


Fig. 16. Measured and simulated broadside radiation patterns of the transmit lens array at 475 GHz.

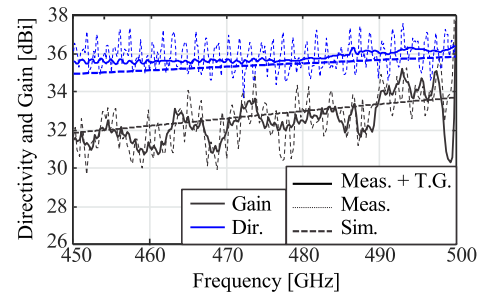


Fig. 17. Measured and simulated directivity and gain as a function of the frequency. Dashed line shows the raw measurement and the solid line shows the time-gated measurement (T.G).

between the different components [31]. This absorber can be interchanged with a horn antenna with a gain of around 20 dB to measure the transmit lens array gain. Since it is a planar near-field scan, a compensation factor of the tilt of the probe has been applied. The compensation of the tilt has been obtained from a full-wave simulation of an open-ended waveguide on a ground plane.

The quasi-optical power distribution antenna is set a few millimeters from the transmit lens array. To align the two, the transmit lens array and the hyperbolic lens are placed on a five-axis motorized stage with a $1.25\ \mu\text{m}$ resolution, independent from the QO power distribution lens antenna.

A. Radiation Pattern and Gain Measurements at Broadside

The radiation patterns were measured in the spot of the hyperbolic lens as it is indicated in Fig. 15 in the WR 2.2 band. The measured one-dimensional (1-D) cuts of the radiation pattern in the E and H planes at 475 GHz of the transmit lens array are shown in Fig. 16. The agreement with the simulations is excellent showing a very directive symmetric main lobe with grating lobe level below -11 dB.

The directivity of the 2-D patterns at the broadside position of the transmit lens array has been measured across the frequency band of 450–500 GHz (see Fig. 17). A time-gating technique has been applied to the measurements to filter out unwanted reflections coming from the antenna measurement setup, as shown in Fig. 17(solid line). The simulated directivity has been computed from the simulated patterns over the measurement

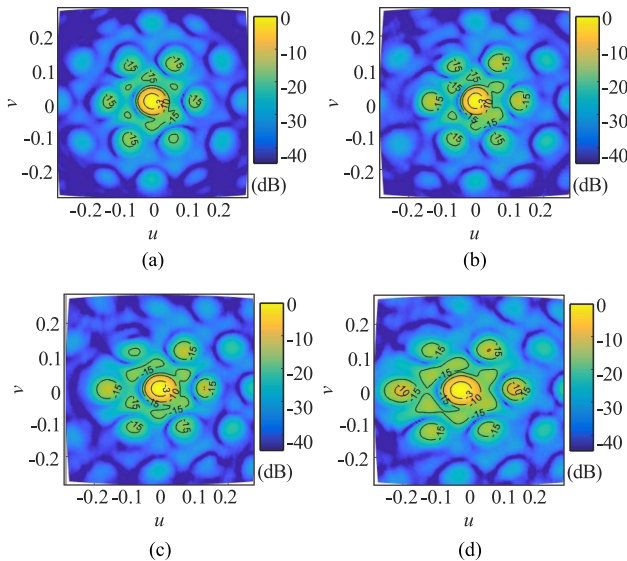


Fig. 18. Measured 2-D radiation patterns of the transmit lens array at 475 GHz for the different scanning angles at (a) broadside, (b) 8.5°, (c) 16.7°, and (d) 25.5°.

scanning area to avoid truncation errors. Overall, the agreement with the simulations is excellent (within 0.5 dB) across the band.

The measured gain is shown in Fig. 17 and it is obtained from the calibrated S_{21} measurement at broadside using a standard diagonal horn antenna and applying the Friis equation. The measured gain is presented without the losses associated to the waveguide block of the quasi-optical power distribution lens (around 3.2 dB) and plastic hyperbolic lens (around 0.75 dB) and the parylene-C matching layer loss (1.6 dB per lens array measured in [32]). The simulated gain has been computed from the transmit lens array efficiency η_{TA} presented in Fig. 10, $G_{sim} = \frac{4\pi A_{TA}}{\lambda^2} \eta_{TA}$. Overall, the measured gain oscillates within 1.5 dB of the simulated gain, validating the semianalytical model presented in Section III and the technological implementation of the proposed transmit lens array.

B. Beam-Steering Measurements

The beam-steering capabilities of the transmit lens array were characterized by displacing the top lens array relative to the waveguide array using the piezo-electric motor. In this demonstration without phase shifters, the positions scanned were the ones corresponding to the array factor grating lobes, as explained in Section I. As illustrated in Fig. 4, the scanned positions will vary as a function of the frequency due to the dispersive behavior of the array factor.

Using this prototype, we were able to measure four scanning positions, i.e., from broadside up to around 25.6° (see Fig. 4). The optimal scanning position was found around the calculated position using the piezo-electric motor. The measured 2-D patterns of the broadside, first grating lobe (8.5°), second grating lobe (16.7°), and third grating lobe (25.6°) directions at 475 GHz are shown in Fig. 18(a)–(d), respectively. It can be observed how the side-lobes are below the -10 dB range and go up to the

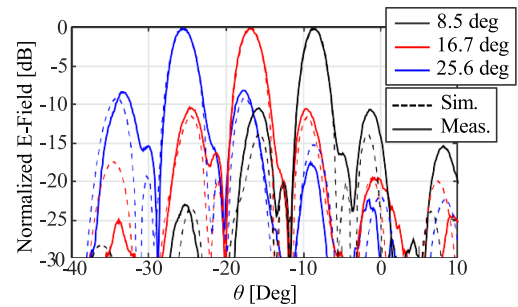


Fig. 19. Measured and simulated scanned radiation patterns of the transmit lens array at 475 GHz.

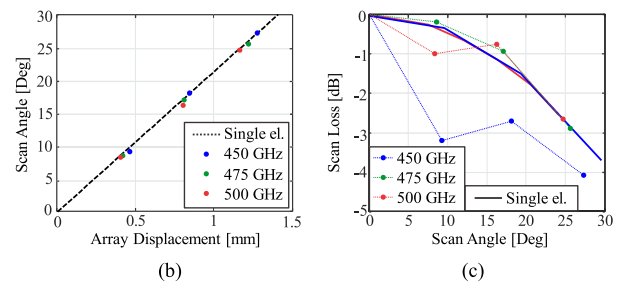
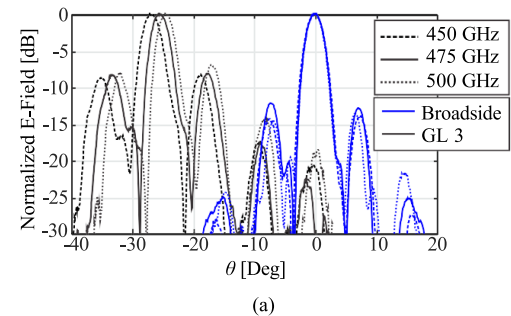


Fig. 20. (a) H plane cut of the measured radiation patterns of the transmit lens array at broadside and the 25.6° scan angle. (b) Beam scanning angle versus lens array displacement. (c) Measured gain scan loss normalized to the broadside case at frequencies 450 GHz, 475 GHz, and 500 GHz.

–8.5 dB range for the third grating lobe scan at 25.6°. Fig. 19 shows the measured 1-D radiation patterns in the scanned plane for the three scanned positions at 475 GHz. The agreement with the simulations, is fair, considering the fact that the simulations do not consider the effect of the multiple reflections inside the lens array.

Since the array factor grating lobe position change as a function of the frequency, the position of the piezo was optimized to find its maximum for 450 GHz, 475 GHz, and 500 GHz independently. The same aforementioned alignment technique was used for each frequency band. The 1-D patterns of the third array factor grating lobe (around 25.6°) are shown in Fig. 20(a) for each frequency. As expected, the third grating lobe displays the highest dispersion, showing an angular variation of 2.5° for a variation in frequency from 450 GHz to 500 GHz.

The displacement of the lens versus the scan angle for the three frequencies is shown in Fig. 20(b). As it can be observed, it follows an $f_{\#}$ in-between 1.6–1.8, as expected from the single element scanning performance. The scan loss versus the scan

angle is shown in Fig. 20(c) for the three different frequencies. Overall, the agreement with simulations is fair, following the element pattern behavior as expected.

VI. CONCLUSION

We presented a transmit lens array with beam-steering capabilities that is fed coherently using a QO power distribution for submillimeter wavelengths. The design has been optimized with a semianalytical model that allows us to calculate the performance of the QO power distribution and lens transmit array. By using the evaluation of antennas in reception methodology, the transmit lens array performance can be obtained from the computation of the QO power coupling efficiency, the impedance matching efficiency and the aperture efficiency of the transmit lens array. A seven-element transmit lens array using the leaky-wave lens antennas developed in [12] has been optimized, achieving 60% QO coupling, 80% of aperture efficiency, and >90% matching efficiency.

A prototype working in the 450–650 GHz band has been fabricated using a combination of laser, diamond-turning, and DRIE micromachining technologies in silicon. A piezo-electric motor has been integrated in the transmit array translating the lens-phased array and steer the 35 dBi beam up to 25°. A very good agreement between the measured and simulated performance has been achieved, validating the semianalytical model of the transmit lens array. These promising results demonstrate the capabilities to achieve a high-gain and low-profile front-end architecture that achieves steering capabilities over a large bandwidth at submillimeter wavelengths.

APPENDIX SILICON LENS WAFER STACKS

Initially, the same lens arrays as in [12] were used for this prototype, including the lens spacers that were formed of five 1 mm thick wafers and three 300 μm thick wafers. The leaky-lens feed was refabricated to be included in the array configuration (in [12] was only demonstrated for a single pixel) and in a new metal fixture. Overall, the complete transmit lens array consisted on 23 layers, 11 for the lens phased array, and 11 layer for the bottom array and one for the waveguide array. All the layers were aligned using the pensile silicon pins and glued together as in [12]. Measurements of this prototype were realized on the same measurement setup detailed in the Section IV.

However, the initial measurement results were not consistent with expectations from simulations. Strong ripples were present in the frequency measurements of the radiation patterns. An example is shown in Fig. 21, where the directivity of the array pattern is plotted against the frequency. This effect was not observed in our previous prototype [12], since that prototype had less layers and a smaller measurement bandwidth. For the present work, the measurements were realized using commercial frequency extenders covering the entire WR2.2 band. After inspecting to the wafer stacks under the microscope, we realized that few of the layers contained gaps in the order of tens of microns. Even after trying to reassemble the stacks multiple times, it was nearly impossible to prevent some sort of gap in

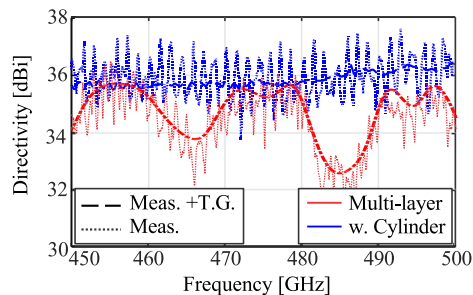


Fig. 21. Measured directivity for the multilayer based lens array assembly compared with the cylinder based lens array assembly. Dotted line shows the raw measurement and the dashed line shows the time-gated measurement (T.G).

the stack. Thus, we decided to substitute the wafer stack that synthesized the lens height with a solid piece of high-resistivity silicon. With this, we reduced the number of layers by half, needing only nine layers in total.

Thus, to corroborate this suspicion, a new assembly was realized using high resistivity cylinders of 19.2 mm diameter and 5.9 mm thick as the lens spacer. The directivity measured using this prototype is also shown in Fig. 21. Indeed, the large ripples are gone and after time-gating to remove environmental and setup-related effects, the line is nearly straight. All other measurements presented in this article were performed on the new assembly with the cylinder silicon block.

ACKNOWLEDGMENT

Part of this work was carried out at the Jet Propulsion Laboratory, California Institute of Technology, Pasadena, CA, USA, under a contract with the National Aeronautics and Space Administration.

REFERENCES

- [1] P. H. Siegel, "THz instruments for space," *IEEE Trans. Antennas Propag.*, vol. 55, no. 11, pp. 2957–2965, Nov. 2007, doi: [10.1109/TAP.2007.908557](https://doi.org/10.1109/TAP.2007.908557).
- [2] R. E. Cofield and P. C. Stek, "Design and field-of-view calibration of 114–660-GHz optics of the Earth observing system microwave limb sounder," *IEEE Trans. Geosci. Remote Sens.*, vol. 44, no. 5, pp. 1166–1181, May 2006, doi: [10.1109/TGRS.2006.873234](https://doi.org/10.1109/TGRS.2006.873234).
- [3] M. Kotiranta, K. Jacob, H. Kim, P. Hartogh, and A. Murk, "Optical design and analysis of the submillimeter-wave instrument on JUICE," *IEEE Trans. Terahertz Sci. Technol.*, vol. 8, no. 6, pp. 588–595, Nov. 2018, doi: [10.1109/TTHZ.2018.2866116](https://doi.org/10.1109/TTHZ.2018.2866116).
- [4] S. Gulkis et al., "Remote sensing of a comet at millimeter and submillimeter wavelengths from an orbiting spacecraft," *Planet. Space Sci.*, vol. 55, no. 9, pp. 1050–1057, 2007.
- [5] G. Chattopadhyay, "Terahertz instruments for CubeSats," in *Proc. IEEE Microw. Theory Techn. Soc. Int. Microw. RF Conf.*, 2017, pp. 1–5, doi: [10.1109/IMaRC.2017.8449669](https://doi.org/10.1109/IMaRC.2017.8449669).
- [6] Y. Yang, O. D. Gurbuz, and G. M. Rebeiz, "An eight-element 370–410-GHz phased-array transmitter in 45-nm CMOS SOI with peak EIRP of 8–8.5 dBm," *IEEE Trans. Microw. Theory Techn.*, vol. 64, no. 12, pp. 4241–4249, Dec. 2016.
- [7] K. Guo, Y. Zhang, and P. Reynaert, "A 0.53-THz subharmonic injection-locked phased array with 63- μW radiated power in 40-nm CMOS," *IEEE J. Solid-State Circuits*, vol. 54, no. 2, pp. 380–391, Feb. 2019, doi: [10.1109/JSSC.2018.2877203](https://doi.org/10.1109/JSSC.2018.2877203).
- [8] Y. Zhao et al., "A 0.54–0.55 THz 2×4 coherent source array with EIRP of 24.4 dBm in 65nm CMOS technology," in *Proc. IEEE Microw. Theory Techn. Soc. Int. Microw. Symp.*, 2015, pp. 1–3, doi: [10.1109/MWSYM.2015.7166806](https://doi.org/10.1109/MWSYM.2015.7166806).

- [9] U. R. Pfeiffer et al., "A 0.53 THz reconfigurable source module with up to 1 mW radiated power for diffuse illumination in terahertz imaging applications," *IEEE J. Solid-State Circuits*, vol. 49, no. 12, pp. 2938–2950, Dec. 2014, doi: [10.1109/JSSC.2014.2358570](https://doi.org/10.1109/JSSC.2014.2358570).
- [10] I. Mehdi, J. Siles, C. Lee, and R. Lin, "Compact Submillimeter-wave multi-pixel local oscillator sources," in *Proc. 40th Int. Conf. Infrared, Millimeter, Terahertz Waves*, 2015, pp. 1–2, doi: [10.1109/IRMMW-THz.2015.7327567](https://doi.org/10.1109/IRMMW-THz.2015.7327567).
- [11] T. Reck et al., "A silicon micromachined eight-pixel transceiver array for submillimeter-wave radar," *IEEE Trans. Terahertz Sci. Technol.*, vol. 5, no. 2, pp. 197–206, Mar. 2015.
- [12] M. Alonso-delPino, S. Bosma, C. Jung-Kubiak, G. Chattopadhyay, and N. Llombart, "Wideband multimode leaky-wave feed for scanning lens-phased array at submillimeter wavelengths," *IEEE Trans. Terahertz Sci. Technol.*, vol. 11, no. 2, pp. 205–217, Mar. 2021, doi: [10.1109/TTHZ.2020.3038033](https://doi.org/10.1109/TTHZ.2020.3038033).
- [13] S. Bosma, N. Van Rooijen, M. Alonso-Delpino, M. Spirito, and N. Llombart, "First demonstration of dynamic high-gain beam steering with a scanning lens phased array," *IEEE J. Microw.*, vol. 2, no. 3, pp. 419–428, Jul. 2022, doi: [10.1109/JMW.2022.3179953](https://doi.org/10.1109/JMW.2022.3179953).
- [14] S. Rahiminejad et al., "A low-loss silicon MEMS phase shifter operating in the 550-GHz band," *IEEE Trans. Terahertz Sci. Technol.*, vol. 11, no. 5, pp. 477–485, Sep. 2021, doi: [10.1109/TTHZ.2021.3085123](https://doi.org/10.1109/TTHZ.2021.3085123).
- [15] M. Alonso-delPino, C. Jung-Kubiak, T. Reck, N. Llombart, and G. Chattopadhyay, "Beam scanning of silicon lens antennas using integrated piezo-motors at submillimeter wavelengths," *IEEE Trans. Terahertz Sci. Technol.*, vol. 9, no. 1, pp. 47–54, Jan. 2019, doi: [10.1109/TTHZ.2018.2881930](https://doi.org/10.1109/TTHZ.2018.2881930).
- [16] M. Alonso-del Pino, C. Jung-Kubiak, T. Reck, C. Lee, and G. Chattopadhyay, "Micromachining for advanced terahertz: Interconnects and packaging techniques at terahertz frequencies," *IEEE Microw. Mag.*, vol. 21, no. 1, pp. 18–34, Jan. 2020, doi: [10.1109/MMM.2019.2945157](https://doi.org/10.1109/MMM.2019.2945157).
- [17] W. Deal et al., "THz monolithic integrated circuits using InP high electron mobility transistors," *IEEE Trans. Terahertz Sci. Technol.*, vol. 1, no. 1, pp. 25–32, Sep. 2011, doi: [10.1109/TTHZ.2011.2159539](https://doi.org/10.1109/TTHZ.2011.2159539).
- [18] T. J. Reck, C. Jung-Kubiak, J. Gill, and G. Chattopadhyay, "Measurement of silicon micromachined waveguide components at 500–750 GHz," *IEEE Trans. Terahertz Sci. Technol.*, vol. 4, no. 1, pp. 33–38, Jan. 2014, doi: [10.1109/TTHZ.2013.2282534](https://doi.org/10.1109/TTHZ.2013.2282534).
- [19] H.-T. Zhu et al., "A micromachined 1.37 THz waveguide-based 2 × 2 beam divider," *IEEE Trans. Terahertz Sci. Technol.*, vol. 12, no. 6, pp. 565–573, Nov. 2022, doi: [10.1109/TTHZ.2022.3200208](https://doi.org/10.1109/TTHZ.2022.3200208).
- [20] B. Mirzaei et al., "Efficiency of multi-beam Fourier phase gratings at 1.4 THz," *Opt. Exp.*, vol. 25, pp. 6581–6588, 2017.
- [21] Y. Gan et al., "81 supra-THz beams generated by a Fourier grating and a quantum cascade laser," *Opt. Exp.*, vol. 27, pp. 34192–34203, 2019.
- [22] Y. Gan et al., "Bandwidth of a 4.7 THz beam multiplexer based on Fourier grating," *J. Opt.*, vol. 24, no. 6, 2022, Art. no. 064006.
- [23] M. Alonso-DelPino, S. Bosma, C. Jung-Kubiak, G. Chattopadhyay, and N. Llombart, "Broadband power distribution using multi-mode leaky-wave lens antennas at submillimeter wavelengths," in *Proc. 46th Int. Conf. Infrared, Millimeter Terahertz Waves*, 2021, pp. 1–1, doi: [10.1109/IRMMW-THz50926.2021.9567576](https://doi.org/10.1109/IRMMW-THz50926.2021.9567576).
- [24] M. Alonso-delPino et al., "Demonstration of a broadband quasi-optical power distribution and beam-steering with transmit lens arrays at 550 GHz," in *Proc. 47th Int. Conf. Infrared, Millimeter Terahertz Waves*, 2022, pp. 1–2, doi: [10.1109/IRMMW-THz50927.2022.9895904](https://doi.org/10.1109/IRMMW-THz50927.2022.9895904).
- [25] M. Alonso-delPino et al., "Integrated silicon lens-antenna based on a top-hat leaky-wave feed for quasi-optical power distribution at THz frequencies," in *Proc. IEEE Microw. Theory Techn. Soc. Int. Microw. Symp.*, 2023, pp. 303–306.
- [26] K. Kuliabin, C. M. Blasini, R. Lozar, S. Chartier, and R. Quay, "A 220–300 GHz vector modulator in 35 nm GaAs mHEMT technology," in *Proc. IEEE/Microw. Theory Techn. Soc. Int. Microw. Symp.*, 2023, pp. 299–302, doi: [10.1109/IMS37964.2023.10188185](https://doi.org/10.1109/IMS37964.2023.10188185).
- [27] M. Alonso-delPino, T. Reck, C. Jung-Kubiak, C. Lee, and G. Chattopadhyay, "Development of silicon micromachined microlens antennas at 1.9 THz," *IEEE Trans. Terahertz Sci. Technol.*, vol. 7, no. 2, pp. 191–198, Mar. 2017, doi: [10.1109/TTHZ.2017.2655340](https://doi.org/10.1109/TTHZ.2017.2655340).
- [28] M. A. Campo, D. Blanco, S. Bruni, A. Neto, and N. Llombart, "On the use of fly's eye lenses with leaky-wave feeds for wideband communications," *IEEE Trans. Antennas Propag.*, vol. 68, no. 4, pp. 2480–2493, Apr. 2020, doi: [10.1109/TAP.2019.2952474](https://doi.org/10.1109/TAP.2019.2952474).
- [29] M. Alonso-DelPino et al., "Design guidelines for a terahertz silicon microlens antenna," *IEEE Antennas Wireless Propag. Lett.*, vol. 12, pp. 84–87, 2013, doi: [10.1109/LAWP.2013.2240252](https://doi.org/10.1109/LAWP.2013.2240252).
- [30] C. Jung-Kubiak et al., "A multistep DRIE process for complex terahertz waveguide components," *IEEE Trans. Terahertz Sci. Technol.*, vol. 6, no. 5, pp. 690–695, Sep. 2016.
- [31] A. Gonzalez, "Probe characterization in terahertz near-field beam measurement systems," *IEEE Trans. Terahertz Sci. Technol.*, vol. 6, no. 6, pp. 824–831, Nov. 2016, doi: [10.1109/TTHZ.2016.2607522](https://doi.org/10.1109/TTHZ.2016.2607522).
- [32] J. Bueno, S. Bosma, T. Bußkamp-Alda, M. Alonso-delPino, and N. Llombart, "Lossless matching layer for silicon lens arrays at 500 GHz using laser ablated structures," *IEEE Trans. Terahertz Sci. Technol.*, vol. 12, no. 6, pp. 667–672, Nov. 2022, doi: [10.1109/TTHZ.2022.3202031](https://doi.org/10.1109/TTHZ.2022.3202031).



Maria Alonso-delPino (Senior Member, IEEE) received the degree in telecommunications engineering from the Technical University of Catalonia (UPC), Barcelona, Spain, in 2008; the M.S. degree in electrical engineering from the Illinois Institute of Technology, Chicago, IL, USA, in 2008, and the Ph.D. degree in signal theory and communications/electrical engineering from UPC in 2013.

From 2014 to 2015, she was as a Postdoctoral Researcher with the Technical University of Delft (TUDelft), Delft, The Netherlands. From 2015 to 2016, she was a NASA Postdoctoral Fellow with the Jet Propulsion Laboratory (JPL), Pasadena, CA, USA. From 2016 to 2020, she was a Member of the Technical Staff at the Sub-millimeter Wave Advanced Technology Group of JPL/NASA. Since 2020, she has been an Assistant Professor with TUDelft. Her research interests include millimeter and submillimeter-wave heterodyne and direct detection technologies, antennas, and quasi-optical systems.

Dr. Alonso-delPino was the recipient of the Outstanding Reviewer Award of the IEEE TRANSACTIONS ON TERAHERTZ SCIENCE AND TECHNOLOGY in 2013, 2014 IEEE Terahertz Science and Technology Best Paper award, and Best Antenna Design Paper award of the 2022 European Conference on Antennas and Propagation (EuCAP).



Sjoerd Bosma (Member, IEEE) received the M.Sc. (*cum laude*) and the Ph.D. (*cum laude*) degrees in electrical engineering from the Delft University of Technology, Delft, The Netherlands, in 2017 and 2023, respectively.

His Ph.D. project focused on scanning lens phased array antennas at sub-millimeter wavelengths. This project was in collaboration with NASA's Jet Propulsion Laboratory, Pasadena, CA, USA, where he spent five months in the Submillimeter-Wave Advanced Technology group as a Visiting Student Researcher in 2018 and 2019. His Ph.D. research has led to more than 30 journal and conference contributions and four best-paper nominations. He currently works with NXP Semiconductors, Eindhoven, The Netherlands, on the next generation of automotive radars.



Cecile Jung-Kubiak (Senior Member, IEEE) received the M.S. degree in physics and materials chemistry from Polytech Montpellier, Montpellier, France, in 2006, and the Ph.D. degree in physics from Université Paris-Sud XI, Orsay, France, in 2009.

She is currently the Technical Group Lead for Advanced Microsensors and Microsystems, Jet Propulsion Laboratory, Pasadena. She has coauthored more than 100 papers in international journals and conferences and holds nine patents. Her research interests include the development of silicon-based micro-instruments, the miniaturization of multipixel arrays at THz frequencies, and micro-electrospray propulsion systems.

Dr. Jung-Kubiak was a recipient of the two-year NASA Postdoctoral Fellowship from the California Institute of Technology, Pasadena, CA, USA, in 2010, 2020 NASA Early Career Public Achievement Medal, 2018 JPL Lew Allen Award, 2014 IEEE Terahertz Science and Technology Best Paper Award, and the 2010 JPL Outstanding Postdoctoral Research Award in the field of technology, instrumentation, and engineering.



Juan Bueno received the graduation degree in physics from the University of Cantabria, Santander, Spain, in 2003, and the Ph.D. degree in physics from the University of Leiden, Leiden, The Netherlands, in 2007.

During his Ph.D. degree, he studied quantum crystals at very low temperatures. From 2007 to 2008, he was a Postdoctoral Fellow with the University of California, San Diego, CA, USA, continuing his work on quantum crystals. In 2008, he switched his research topics and interests from fundamental physics to the study of superconducting devices. Until 2010, he was a Postdoctor with Jet Propulsion Laboratory (JPL), Pasadena, CA, USA. During this time, he pioneered a new type of pair-breaking radiation detector, the quantum capacitance detector. After his time with JPL, he joined the Center for Astrobiology, Madrid, Spain, in 2010, working mainly on kinetic inductance detectors (KIDs). He became an Instrument Scientist in 2012 with SRON, Netherlands Institute for Space Research, Leiden, The Netherlands, working on the development of KIDs for submillimeter wave and far IR space-based observatories. In 2021, he became a high-frequency RF Engineer with ELCA Group, Technical University of Delft, Delft, The Netherlands, working on the XG sensing and communications laboratories. He has authored or coauthored more than 50 peer-reviewed papers, a fourth of them as the first author, and more than 40 peer-reviewed papers, almost a third of them as the first author. His research focuses on the development of over the air technology at submillimeter wave frequencies for detection and communication applications.

Dr. Bueno was the recipient of NASA Postdoctoral position and the JAE-doc grant.



Goutam Chattopadhyay (Fellow, IEEE) received the Ph.D. degree in electrical engineering from the California Institute of Technology (Caltech), Pasadena, CA, USA, in 2000.

He is currently a Senior Research Scientist with the NASA's Jet Propulsion Laboratory, Caltech, CA, USA, where he is a Visiting Associate with the Division of Physics, Mathematics, and Astronomy. He has authored and coauthored more than 350 publications in international journals and conferences and holds more than 20 patents. His research interests include

microwave, millimeter-wave, terahertz receiver systems and radars, and development of space instruments.

Dr. Chattopadhyay is the recipient of more than 35 NASA technical achievements and new technology invention awards, including IEEE Region 6 Engineer of the Year Award in 2018 and distinguished Alumni Award from the Indian Institute of Engineering Science and Technology, India, in 2017. He was also the recipient of the Best Journal Paper Award in 2013 and 2020 by IEEE TRANSACTIONS ON TERAHERTZ SCIENCE AND TECHNOLOGY, Best Paper Award for antenna design and applications at the European Antennas and Propagation conference in 2017, IETE Biman Bihari Sen Memorial Award in 2022, and Prof. S. N. Mitra Memorial Award in 2014. He is a Fellow of the Institution of Electronics and Telecommunication Engineers, India, and an IEEE Distinguished Lecturer. He is an elected AdCom Member of the IEEE Microwave Theory and Techniques Society, the Chair of the Membership and Geographic Activities Committee, and Past Chair of the Meetings and Symposium Committee.



Nuria Llombart (Fellow, IEEE) received the master's degree in electrical engineering and the Ph.D. degree from the Polytechnic University of Valencia, Valencia, Spain, in 2002 and 2006, respectively.

During her master's degree studies, she spent one year with the Friedrich Alexander University of Erlangen Nuremberg, Erlangen, Germany, and was with the Fraunhofer Institute for Integrated Circuits, Erlangen, Germany. From 2002 to 2007, she was with the Antenna Group, TNO Defense, Security and Safety Institute, The Hague, The Netherlands, working as a

Ph.D. student and afterwards as a Researcher. From 2007 to 2010, she was a Postdoctoral Fellow with the California Institute of Technology, working with the Submillimeter Wave Advance Technology Group, Jet Propulsion Laboratory, Pasadena, CA, USA. She was a "Ramón y Cajal" fellow in the Optics Department, Complutense University of Madrid, Madrid, Spain, from 2010 to 2012. In September 2012, she was with the THz Sensing Group, Technical University of Delft, Delft, The Netherlands, where as of February 2018 she was a Full Professor. She has coauthored more than 200 journal and international conference contributions in the areas of antennas and THz systems.

Dr. Llombart was the recipient H. A. Wheeler Award for the Best Applications Paper of 2008 in the IEEE TRANSACTIONS ON ANTENNAS AND PROPAGATION, the 2014 THz Science and Technology Best Paper Award of the IEEE Microwave Theory and Techniques Society, and several NASA awards. She was also the recipient of the 2014 IEEE Antenna and Propagation Society Lot Shafai Mid-Career Distinguished Achievement Award. She is as a Board member of the IRMMW-THz International Society and Associate Editor for the IEEE TRANSACTION ON ANTENNAS AND PROPAGATION. In 2015, she was the recipient of European Research Council Starting Grant. In 2019, she became IEEE Fellow for contributions to millimeter and submillimeter wave quasi-optical antennas.